Chapter 6

DC-Link Control Schemes in Multilevel Converters for WECS

Carlos A. Reusser

Additional information is available at the end of the chapter

http://dx.doi.org/10.5772/intechopen.72360

Abstract

The introduction of renewable energy resources since the late 1990s as an alternative to fossil energies has impact the development of wind energy and its integration to the grid. From the early 2000s, the wind energy has positioned itself as the most grown-up energy market in the world. This fact has introduced the need to deal with increasing power demands with limited generation capabilities, in terms of generator power density, for low rotation speeds and medium voltage generation within a grid interconnection in high voltage, and other grid code demands, like THD, power factor regulation, and the requirement of continuous operation under faulty condition. Until today, this issue has been solved using classical power converter topologies, using three-level voltage source converters (3LVSC) or multilevel configurations, such as neutral point clamped and cascaded H-Bridge topologies. In this chapter, the main advantages and drawbacks of classical multilevel converter topologies are analyzed, in terms of their DC-link voltage stability capability and different approaches to DC-link control and to new converter topologies, derived from classical topologies, are presented and compared with simulation results.

Keywords: multilevel converter, neutral point clamped, cascaded H-Bridge, modulation strategy, control scheme, voltage drift, model predictive control

1. Introduction

In the past decade, renewable energies like wind and solar energies have increased their participation in the global energy matrix, increasing from a 10% of the global energy market in 1993 to an 11% in 2011 with an estimated 16% in 2020. This in despite of fossil energies, which are experimenting a decrease with the passing years [1]. Among these resources, wind energy conversion systems have emerged as the leader at the present time. According to the

Global Wind Energy Council (GWEC) annual report, over 27 [*GW*] of new wind power generation capacity came online worldwide in 2008 representing a 36% growth rate in the annual market, bringing the total global wind power capacity to over 383 [*GW*] through the end of 2013. According to the global energy status report presented by the Global Wind Energy Council (GWEC), during the period 2015–2016, the installed capacity of renewable energies has experienced an estimated growth of around 47 [*GW*] on its total installed capacity. In these orders, the total worldwide installed power is capable to supply about a 23.7% of the global energy demands, representing half of the global demand growth. These facts have positioned wind energy as the leading energy source with a growth of 63 [*GW*] for the same period (**Figure 1**).

This indicates that there is a growing global demand for emissions-free wind power, which can be installed quickly, virtually everywhere in the world, making wind energy conversion one of the fastest growing sources of new electric generation.

From a technology point of view, an estimated of 330 manufacturers for commercial WECS have been identified in at least 40 countries [2], and another 300 are technology suppliers for parts, consulting and sales services. This development and maturity reached by the industry have among other drivers, cost reduction, increased efficiency, reliability and proprietary technology development.

One of the key technologies in WECS that has experienced extensive innovation in the last decade is the generator and power converter interface to the grid. Configurations have moved

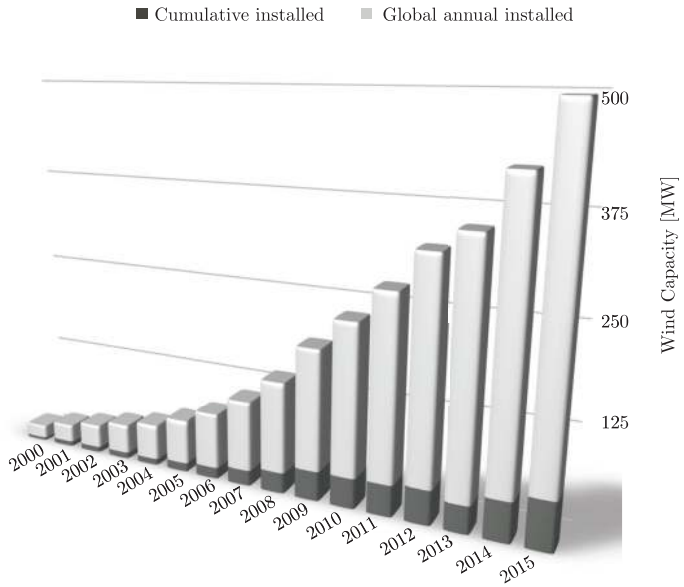

Figure 1. WECS penetration.

from fixed speed induction generators, going through partial capacity converter stage in doubly fed induction generators, to full-capacity converters used in synchronous generators (with wound rotor and permanent magnet rotor) [3]. They can be further divided depending if they feature a gearbox or not (gearless or direct-dive) or even a reduced gearbox (one stage). Combinations of different configuration types, generators, power converters and gear options have resulted in several commercial turbines and proprietary technology [3, 4]. In **Figure 2**, the possible configurations for a WECS solution are presented.

1.1. Fixed-speed WECS

Fixed-speed configurations were introduced in the 1980s, and they are equipped with squirrel cage induction generators (SCIG) or wound rotor induction generators (WRIG), connected directly to the grid. They are designed to obtain maximum efficiency at rated wind speed. In a fixed-speed WECS, the turbine speed is determined by the grid frequency, the generator pole pair number, the machine slip and the gearbox ratio. A change in the wind speed will not affect

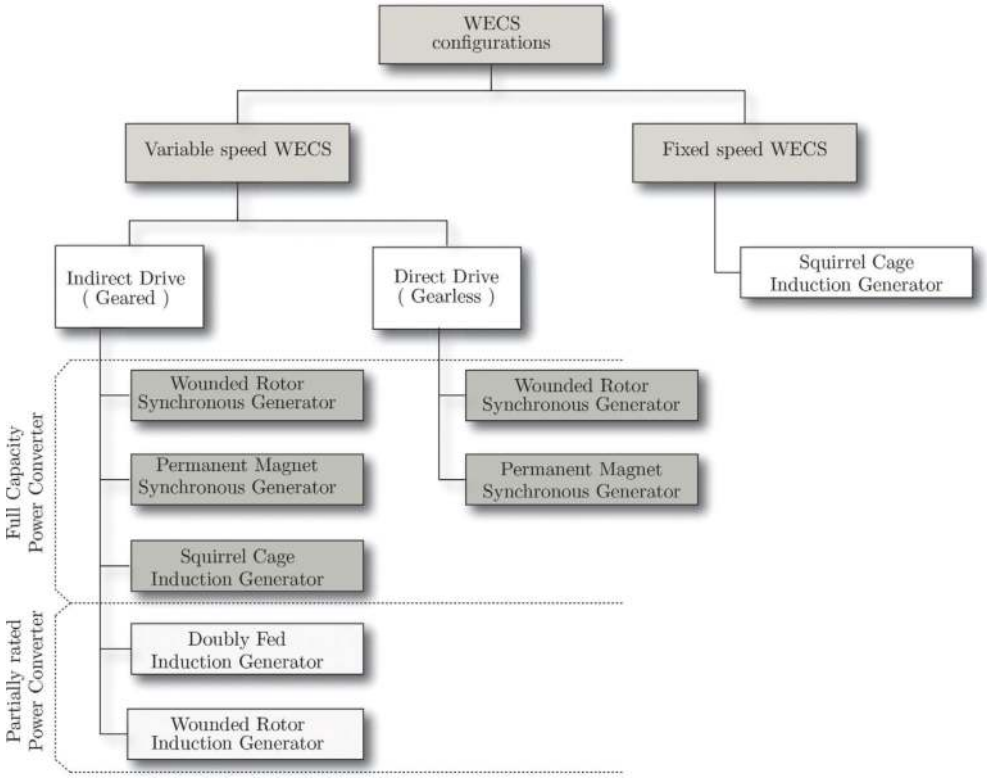

Figure 2. WECS configurations.

the turbine speed to a large extent but will increase the electrical output power. In order to increase the output power, some of these configurations use generators with two sets of windings: one is used for low wind speeds (typically eight pole pairs) and the other for medium and high wind speeds (typically four to six pole pairs).

Power control is achieved aerodynamically either by stall, active stall or pitch control. A soft starter is normally fitted in order to reduce the inrush current during start-ups. Also, a reactive power compensator is needed to reduce the generator reactive power demand as presented in **Figure 3**.

The advantages of this WECS configuration are its simplicity, robustness and reliability. Its drawbacks are the uncontrollable reactive power consumption, mechanical stress and no power quality control [5].

1.2. Variable-speed WECS

Variable-speed configurations were developed first in the 1990s with the introduction of the doubly fed induction generator (DFIG) and the wound rotor induction generator (WRIG). These WECS configurations are designed to achieve maximum electrical power output over a wide range of wind speeds, by using a maximum power point tracking (MPPT) control technique. In this way, the generator rotational speed ω_r is adapted in such a proportion to the wind speed v_s, to keep the turbine tip speed ratio λ[1] corresponding to the turbine maximum performance power.

In the early 2000s, variable speed WECS configuration was extended to the use of wound rotor synchronous generators (WRSG) and permanent magnet synchronous generators (PMSG) including the extended use of multipole and multiphase configurations and full-scale power electronics.

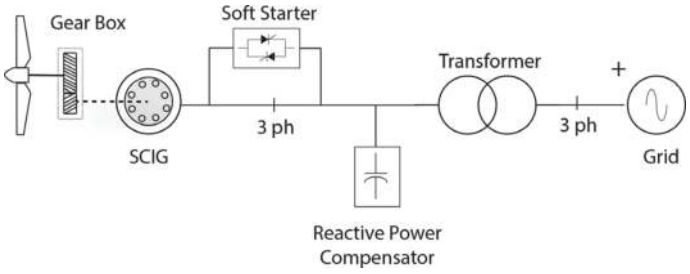

Figure 3. SCIG fixed-speed WECS configuration.

[1]The ratio between the tangential speed of the tip of a blade and the actual velocity of the wind.

Variable speed WECSs are generally divided into two categories, depending on the way of interconnecting the generator to the grid. This are:

1. Partially rated power electronics
2. Full-scale power electronics interfacing wind turbines

1.2.1. Partially rated power electronics

In partially rated power electronics configurations, the generator is connected directly to the grid via a power transformer. The first configuration uses a WRIG fitted with an external resistance, which is controlled by means of power electronics as presented in **Figure 4**. This controlled resistance acts as a dynamic slip controller, and it gives typically a speed range of 2–5%. The power converter has to be designed for handling low voltage but high currents. At the same time, an extra control freedom is obtained at higher wind speeds in order to keep the output power fixed. This solution still needs a soft starter and a reactive power compensator, which is in continuous operation.

The second solution is based on a DFIG generator fitted with back-to-back power converter in parallel as presented in **Figure 5**. This configuration allows full frequency control by controlling the rotor slip, by means of adjusting the rotor winding frequency.

In this case, the power goes from the stator to the grid, while the rotor current is controlled via a four-quadrant back-to-back converter. This configuration enables power flow from stator and rotor to the grid. If the generator is running sub-synchronously, then the electrical power is only delivered into the rotor from the grid. On the other hand, if the generator is running super-synchronously (above the synchronous speed), electrical power is delivered through both, the rotor and the stator, which represents a big improvement respect to the WRIG configuration.

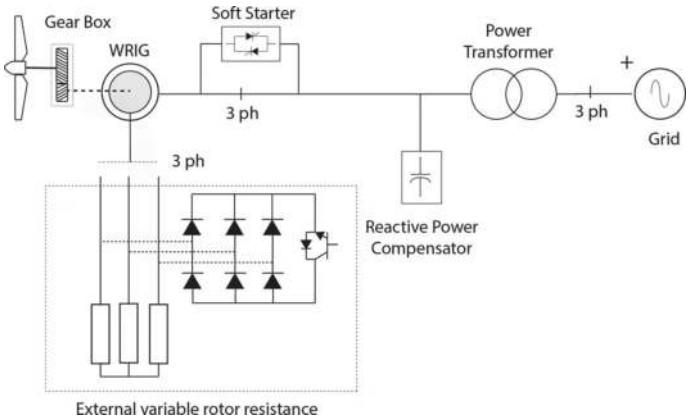

Figure 4. WRIG with external variable resistance configuration.

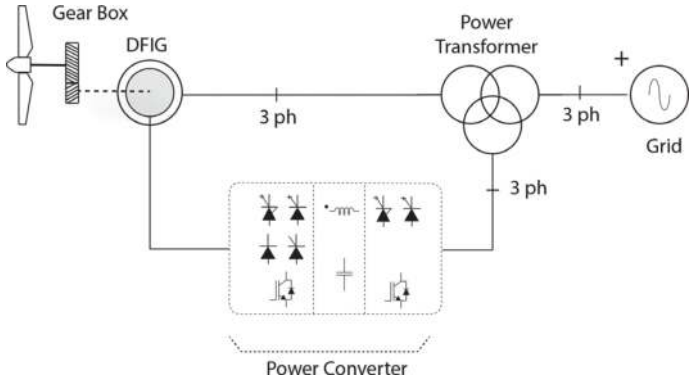

Figure 5. DFIG with partially rated power electronics configuration.

1.2.2. Full-scale power electronics

In the late 2000s, the concept of full-scale power electronics (FSPE) for WECS was introduced. It considers the generator connected to the grid via a power converter. This configuration allows a complete control of the active and reactive power transferred to the utility while operating the generator in its optimum TSR, hence maximum power output. It also has made possible the use of bigger generators, in terms of rated power. As a consequence, wind power conversion has been optimized over the entire speed range, and maintenance costs have been reduced dramatically. Traditional gearbox becomes optional because FSPE allows the wind turbine to work at low speeds. In addition FSPE enables full decoupling between the generator and the grid allowing the implementation of maximum TSR control scheme, for the generator, and voltage-oriented control (VOC) with full active and reactive power control for the inverter stage. These features introduced by FSPE have given WECS the capability to participate actively in grid voltage/frequency regulation, with capability to support the grid under faulty operation conditions (in the range of DC-link voltage stability) [6].

Full-scale power electronics WECS can be implemented in geared or gearless configurations, using squirrel cage induction generators (SCIG), permanent magnet synchronous generators (PMSG) or wound rotor synchronous generators (WRSG) in geared or gearless implementations as presented in **Figure 6**.

2. Control requirements for WECS converter topologies

WECS integration to the grid has also driven to new technological challenges, specifically in the field of wind generator maximum tolerable voltage levels and power converter topologies, for high power ratings. Today, the most accepted solutions for high power ratings are based in variable speed WECS with full-scale power electronics configurations, using multilevel power converters, where back-to-back topologies like neutral point clamped (NPC), active neutral point clamped (ANPC) and cascaded H-Bridge (CHB) converters, shown in **Figure 7**, have

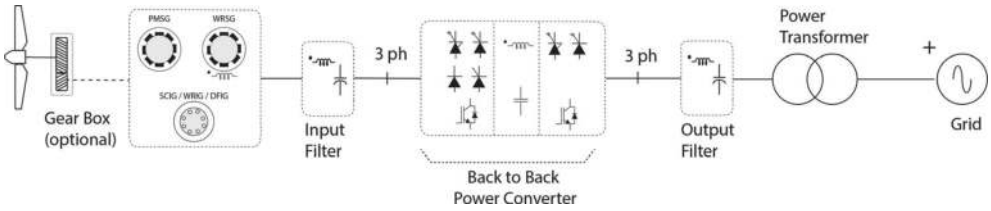

Figure 6. Full-scale power electronics configuration.

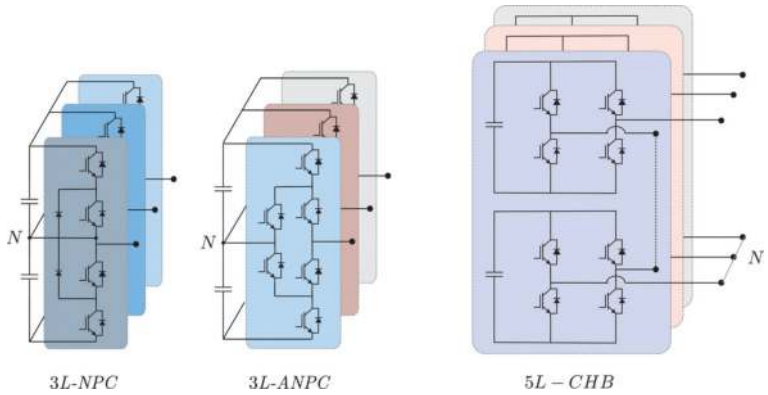

Figure 7. NPC, ANPC and CHB topologies.

become very popular solutions for most large-scale wind-farm projects, because these topologies have reached their technological maturity, proven during the past couple of decades as referred in [7, 8].

In order to serve as a proper generator-grid power flow interface, WECSs have to accomplish with the following control goals, which leave to two different control loops to be analysed:

1. Maximum generator power operation (maximum power tracking control MPPT)
2. DC-link voltage control and balance
3. Grid current control (active and reactive power)

2.1. Generator side control loop

The generator output power depends upon the accuracy to track the different TSR points for a given wind condition as presented in Eq. (1):

$$P_w = \frac{1}{2}\ C_p \rho A \left(\frac{\omega_r r}{\lambda_T}\right)^3 \tag{1}$$

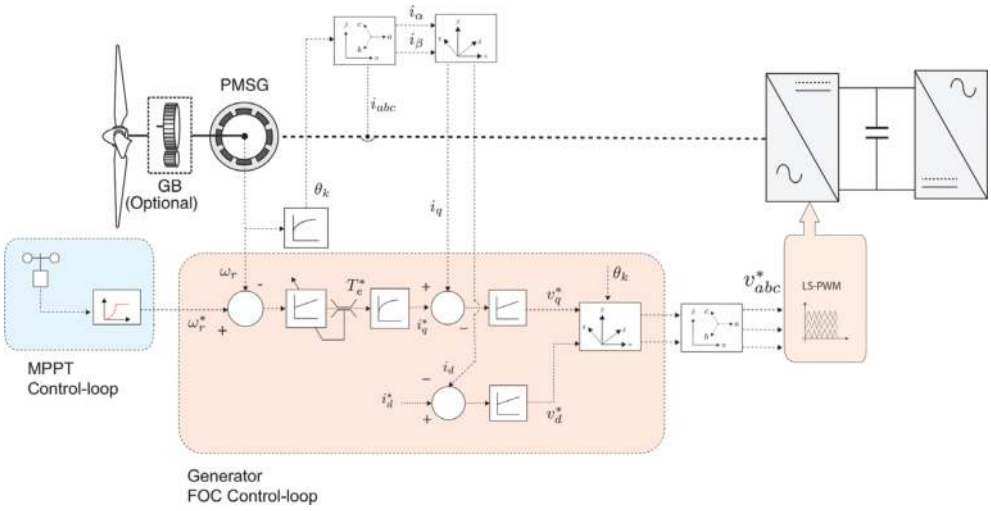

Figure 8. Generator side control scheme.

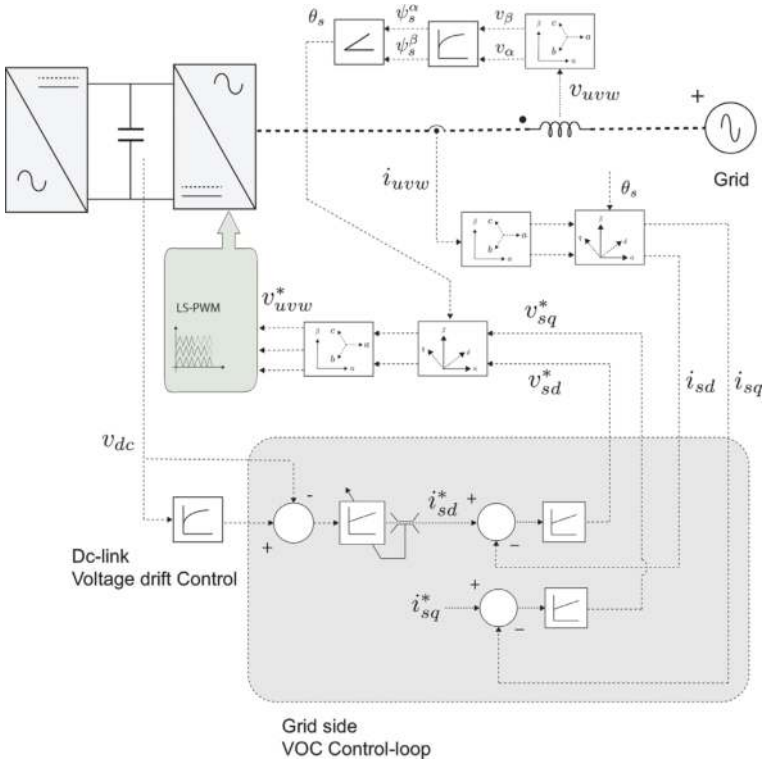

Figure 9. Grid side control scheme.

So as presented previously, the active power delivered by the generator is dependent on λ_T, so maximum active power is reached via a maximum power point tracking (MPPT) control scheme [6, 9, 10]. The control scheme implementation is shown in **Figure 8**.

2.2. Grid side control loop

Grid side control is achieved via active and reactive power control [11, 12]. Active and reactive power delivered to the grid is controlled by the means of power decoupling in the synchronous rotating reference frame dq, which is given by Eqs. (2)–(3). Decoupling is achieved using virtual flux voltage-oriented control (VF-VOC) strategy or via a PLL orientation:

$$P = \frac{3}{2}\,\mathbb{R}e\left\{v^d\left(i^d + ji^q\right)\right\} \tag{2}$$

$$Q = \frac{3}{2}\,\mathbb{I}m\left\{v^d\left(i^d + ji^q\right)\right\} \tag{3}$$

Thus, by setting $i^q = 0$, it is possible to maximize the active power flow into the grid. However, this control scheme requires of a synchronous reference frame orientation θ_k, which is provided by a virtual-flux space vector Ψ_L (4), and its implementation is shown in **Figure 9**:

$$\psi_o^{(\alpha\beta)} = \int_0^t v^{(\alpha\beta)}(\tau)\,d\tau \tag{4}$$

$$\theta_k = atan2\left(\psi_o^{\alpha}, \psi_o^{\beta}\right) \tag{5}$$

3. Power converter DC-link stability

As presented in the previous section in Eqs. (2)–(3), active and reactive power stable power flow, from the generator to the grid, is highly dependent on the DC-link voltage v_d stability. Moreover, DC-link voltage level is directly dependent on the power harvested from the wind speed and stored in the DC-link capacitor and then converted and rejected to the grid and consumer centres. Both stages are controlled by the converter modulation strategy. Thus, the modulation strategy and the converter topology have a preponderant incidence, in the power flow stability and the DC-link voltage stability as a consequence.

In this matter, the main issue for multilevel power converters in FSPE configuration is referred to the fact that most of the time generators will be operating at a fraction of their rated power, so in order to deal with this fact, multilevel converters have to operate within their low modulation index region. This represents a major concern in the case of the NPC and ANPC topologies.

3.1. Modulation strategies

3.1.1. Sinusoidal pulse width modulation (SPWM)

For multilevel topologies, level-shifted PWM (LS-PWM) strategy has become a standard as modulation strategy for these topologies, because it is suitable for any multilevel converter topology and presents low harmonic distortion [13, 14]. The switching pattern for a LS-PWM

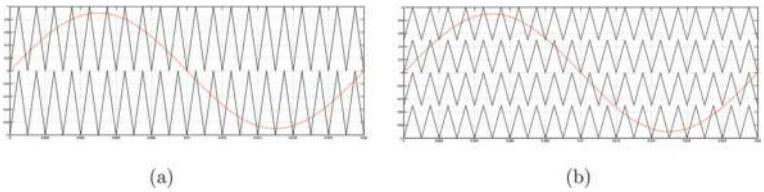

Figure 10. Level-shifted PWM. (a) 3 level converter LS-PWM scheme (b) 5 level converter LS-PWM scheme.

scheme consists of $(\ell - 1)$ triangular carriers and ℓ number of levels to be synthesize, as shown in **Figure 10**.

3.1.1.1. Cascaded H-Bridge topology

The cascaded H-Bridge (CHB) converter consists of an arrangement of series-connected unit cells (per leg), each one consisting an H-Bridge voltage source converter, with isolated DC-sources.

For the 5L-CHB converter basic cell in **Figure 11**, the corresponding switching states are presented in **Table 1** as follows.

The isolated cell structure of the CHB converter and its floating condition with respect to ground prevents the NP current flow; hence, no voltage unbalance on each cell DC-link appears. This is due to the fact that only a single current path is established on each switching cycle. So the energy flow direction is the same for each cell DC-link capacitor.

The main drawback of the CHB converter is the large number of isolated DC supplies and the high number of components.

3.1.1.2. Neutral point clamped topology

Considering the 3L-NPC converter basic cell shown in **Figure 12**, the generated switching states are summarized in **Table 2**.

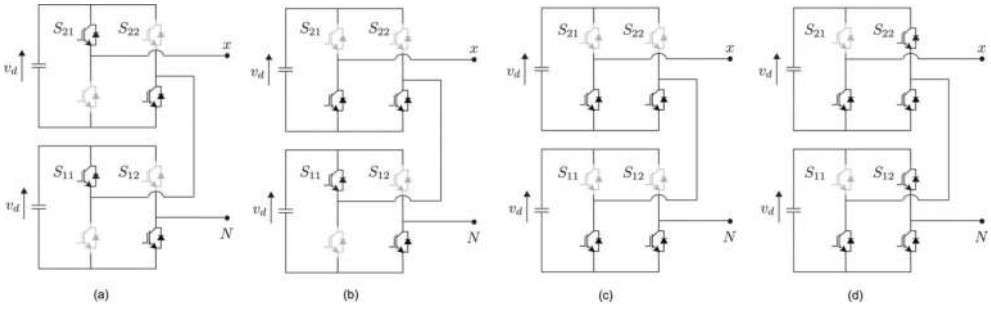

Figure 11. CHB LS-PWM switching states: (a) $2E$ state, (b) E state, (c) zero state and (d) $-2E$ state.

S_{11}	$\overline{S}_{11}$	S_{21}	$\overline{S}_{121}$	v_{xN}
1	0	1	0	$2v_d$
1	0	1	1	v_d
1	0	0	0	
1	1	1	0	
0	0	1	0	
0	0	0	0	0
1	0	1	1	
1	1	0	0	
1	1	1	1	
0	0	0	1	
0	1	1	0	
0	1	1	1	$-v_d$
0	1	0	0	
1	1	0	1	
0	0	0	1	
0	1	0	1	$-2v_d$

Table 1. 5L-CHB switching states per leg using LS-PWM (fundamental cell).

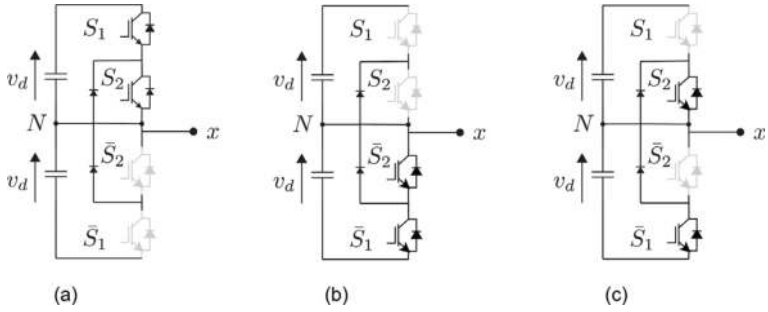

Figure 12. NPC LS-PWM switching states: (a) P state, (b) N state and (c) zero state.

	S_1	$\overline{S}_1$	S_2	$\overline{S}_2$	v_{xN}
P	1	0	1	0	v_d
0	0	1	1	0	0
N	0	1	0	1	$-v_d$

Table 2. 3L-NPC switching states per leg using LS-PWM (fundamental cell).

The main drawback of the neutral point clamped topologies is that depending on the switching state and modulation index, they develop neutral point (NP) circulating currents, which leads to unbalance in the DC-link capacitors, because of an uneven energy flow to and from the DC-link capacitors, driving to unsymmetrical voltages. The NP circulating current i_o can be expressed as in Eqs. (6) and (7):

$$i_o = S_{x0}\, i_x + S_{y0}\, i_y + S_{z0}\, i_z \tag{6}$$

$$S_{x0},\, S_{y0},\, S_{z0} \in [0, 1] \tag{7}$$

where $S_{x0}\, S_{y0}\, S_{z0}$ are the corresponding zero switching states for each phase xyz, given the voltage references as in Eq. (8):

$$\begin{cases} v_x^*(t) = m\ \sin(\omega_s t) \\ v_y^*(t) = m\ \sin\left(\omega_s t - \dfrac{2\pi}{3}\right) \\ v_z^*(t) = m\ \sin\left(\omega_s t + \dfrac{2\pi}{3}\right) \end{cases} \tag{8}$$

where m stands for the modulation index and ω_s the modulating reference frequency; then, the output currents can be expressed as in Eq. (9):

$$\begin{cases} i_x(t) = \hat{I}\sin(\omega_s t + \phi) \\ i_y(t) = \hat{I}\sin\left(\omega_s t - \dfrac{2\pi}{3} + \phi\right) \\ i_z(t) = \hat{I}\sin\left(\omega_s t + \dfrac{2\pi}{3} + \phi\right) \end{cases} \tag{9}$$

with ϕ the power factor corresponding to the operating condition. The duty cycle for switches d_k and $\overline{d}_x$ can be expressed as

$$d_x \begin{cases} m & \sin(\omega t) \quad \omega t \in [0, \pi] \\ 0 & \omega t \in [\pi, 2\pi] \end{cases} \tag{10}$$

$$\overline{d}_k \begin{cases} 1 & \omega t \in [0, \pi] \\ 1 + m & \sin(\omega t) \qquad \omega t \in [\pi, 2\pi] \end{cases} \tag{11}$$

Expressing Eq. (7) in terms of their duty cycles can be expressed as in Eq. (12):

$$i_o = \sum_k \left(d_k - \widehat{d}_k\right) i_k \quad \forall k = x, y, z \tag{12}$$

From Eqs. (8)–(12), the average NP circulating current can be found to be as in Eq. (13):

$$I_o = \ |d_x - \widehat{d}_x|\, i_x + |d_y - \widehat{d}_y|\, i_y + |d_z - \widehat{d}_z|\, i_z \tag{13}$$

As presented in **Figure 13**, the zero switching state establishes a path for which NP current i_o can flow, leading to voltage unbalance in the DC-link capacitors.

A solution for the problem of NP circulating current can be achieved by means of the modulation scheme, in particular by choosing two modulating signals v_{kp} and v_{np} $\forall k = x, y, z$, such that:

$$\begin{cases} v_{kp} = \dfrac{v_k + min\{v_x, v_y, v_z\}}{2} \\ v_{kn} = \dfrac{v_k - max\{v_x, v_y, v_z\}}{2} \end{cases} \tag{14}$$

3.1.2. Space vector modulation (SVM)

3.1.2.1. Neutral point clamped topology

Space vector modulation (SVM) strategy enables the possibility to use some redundant switching states, as presented in **Table 3**.

Due to the nature (type) of each vector, with respect to its corresponding switching state, different voltage space vectors will have different effects on the voltage drift of the DC-link capacitors. This effect can be summarized as follows:

- Zero voltage space vectors v_0 have no effect on voltage deviation.
- Small vectors $V_k \forall k \in [1, \ldots 6]\, k \in \mathbb{Z}$ have a predominant effect on the voltage drift by raising or decreasing the neutral point voltage.
- In Medium vectors $V_k \forall k \in [7, \ldots 12]\, k \in \mathbb{Z}$ in this case, the effect of the switching state cannot been determined exactly, so NP voltage will raise or decrease depending on the system state.
- Large vectors $V_k \forall k \in [12, \ldots 18]\, k \in \mathbb{Z}$ have no influence on the voltage drift.

In order to deal with voltage drift, the dwell time of a small vector can be equally distributed within both redundant switching states, over a sampling period, depending on the sector of

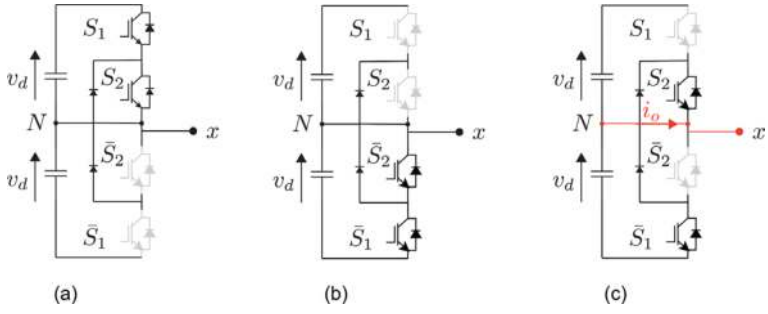

Figure 13. NPC LS-PWM switching states: (a) P state, (b) N state and (c) zero state.

Space vector	Switching state	Type	Magnitude
V_0	[0 0 0]	Zero vector	0
	[P P P]		
	[N N N]		
V_1	[P 0 0]	Small vector	$\frac{1}{3} v_d$
	[0 N N]		
V_2	[P P 0]		
	[0 0 N]		
V_3	[0 P 0]		
	[N 0 N]		
V_4	[0 P P]		
	[N 0 0]		
V_5	[0 0 P]		
	[N N 0]		
V_6	[P 0 P]		
	[0 N 0]		
V_7	[P 0 N]	Medium vector	$\frac{\sqrt{3}}{3} v_d$
V_8	[0 P N]		
V_9	[N P 0]		
V_{10}	[N 0 P]		
V_{11}	[0 N P]		
V_{12}	[P N 0]		
V_{13}	[P N N]	Large vector	$\frac{2}{3} v_d$
V_{14}	[P P N]		
V_{15}	[N P N]		
V_{16}	[N P P]		
V_{17}	[N N P]		
V_{18}	[P N P]		

Table 3. 3L-NPC switching states per leg using SVM (fundamental cell).

the reference space vector. In other words, redundant switching states can be used to minimize the voltage drift effect. However, depending on the reference space vector amplitude (in other words depending on the desired modulation index), the proposed scheme will be more or less effective; thus, when medium vectors are involved, the voltage drift will be a consequence of the load state.

3.1.3. Finite-set model predictive control (FSMPC)

As presented previously, SVM scheme introduces more degrees of freedom, compared to the SPWM method, and as a consequence, redundant switching states are obtained. By selecting

the appropriated space vector and switching sequence, the flow of a neutral point current can be mitigated. However, some switching states have an unknown effect on the NP current, so its effect on the DC-link voltage stability is not clearly defined.

Moreover, SVM leads to high computational cost and complexity, especially when the number of voltage levels increases. It has also to be clarified that due to the unknown behaviour of some switching states in the NP current and the dwell time limitation, the circulating neutral point current is not mitigated at all, as stated in [15, 16].

In order to deal with these constraints, which cannot be solved using classical linear modulation techniques, and to accomplish with the DC-link stability control requirements, finite-set model predictive control (FS-MPC) appears as an available and powerful control scheme, whose control action will select the most appropriated voltage space vector, to fulfil some control goals, via the minimization of a imposed cost function.

The FCS-MPC approach eliminates the need of linear controllers and modulation scheme. This approach is basically an optimization algorithm whose actuation depends on a discrete-time model of the converter switching pattern and its interaction with the load/grid and DC-link. In other words, it depends on how the energy flows from the DC-link to the load/grid and how the voltage on the DC-link is affected by these dynamics.

3.1.3.1. Load/grid model

Considering the converter-grid model presented in **Figure 14**, the following mathematical model given in Eq. (15) can be established:

$$v_{jN}(t) = R_s\, i_j(t) + L_s \frac{d}{dt}\, i_j(t) - e_j(t) \quad \forall j = \{a, b, c\} \tag{15}$$

By rotating the space vector state variables of (15) into a stationary reference frame $\alpha\beta$ and expressing the mathematical model in the state space form, Eqs. (16) and (17) are obtained:

$$\frac{d}{dt}\, i_s^{\alpha}(t) = \frac{1}{L_s}\left[v_s^{\alpha}(t) - e_g^{\alpha}(t) - R\, i_s^{\alpha}(t)\right] \tag{16}$$

$$\frac{d}{dt}\, i_s^{\beta}(t) = \frac{1}{L_s}\left[v_s^{\beta}(t) - e_g^{\beta}(t) - R\, i_s^{\beta}(t)\right] \tag{17}$$

where $v_s^{\alpha}(t)$ and $v_s^{\beta}(t)$ can be expressed in terms of generated voltage space vector $v_s^{\alpha\beta}$ as a function of the switching state S_i and the DC-link voltage v_{dc}, so

$$v_s^{(\alpha\beta)} = f(S_i, v_{dc}, t) \tag{18}$$

$$v_s^{\alpha} = \mathbb{R}\left\{v_s^{(\alpha\beta)}\right\} \tag{19}$$

$$v_s^{\beta} = \mathbb{I}\left\{v_s^{(\alpha\beta)}\right\} \tag{20}$$

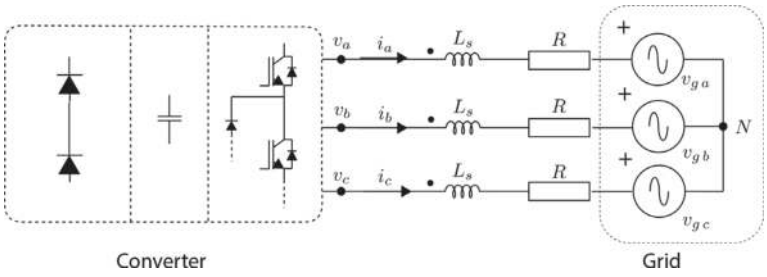

Figure 14. Grid converter model.

The model given in Eqs. (19) and (20) is converted into its discrete-time expression for a given sampling time T_s, approximating the derivative using the backward *Euler* approximation Eq. (21):

$$\frac{d}{dt}x(t) = \frac{x[k+1] - x[k]}{T_s} \tag{21}$$

So the discretised load/grid model in the $\alpha\beta$ stationary reference frame is given in Eqs. (22) and (23):

$$i_s^{\alpha}[k+1] = \Lambda_1\left(v_s^{\alpha}[k] - e_g^{\alpha}[k]\right) + \Lambda_2\, i_s^{\alpha}[k] \tag{22}$$

$$i_s^{\beta}[k+1] = \Lambda_1\left(v_s^{\beta}[k] - e_g^{\beta}[k]\right) + \Lambda_2\, i_s^{\beta}[k] \tag{23}$$

with $\Lambda_1 = \frac{T_s}{L_s}$, $\Lambda_2 = \left(1 - \frac{L_s}{R}T_s\right)$, and the grid voltage space vector $e_g^{(\alpha\beta)}$ can be treated as the system internal perturbation d_i:

$$i_s^{(\alpha\beta)}[k+1] = \Lambda_1(f(S_n, v_{dc}, k) - d_i[k]) + \Lambda_2\, i_s^{(\alpha\beta)}[k] \tag{24}$$

3.1.3.2. DC-link model

The DC-link capacitor voltage dynamics are defined by Eq. (25):

$$i_{dc(\ell)}(t) = C\,\frac{d}{dt}\,v_{dc(\ell)}(t) \quad \forall \ell = \{Up, Low\} \tag{25}$$

The discrete-time model for Eq. (25) can be obtained as in Eq. (26):

$$v_{dc(\ell)}[k+1] = v_{dc(\ell)}[k] + \Gamma\, i_{dc(\ell)}[k] \tag{26}$$

with $\Gamma = \frac{T_s}{C}$; it must be also noted that the capacitor current flow $i_{dc(\ell)}$ is a function of the switching state S_n and the current flow to the load/grid i_s as given in Eq. (27):

$$i_{dc(\ell)} = h(S_i, v_{dc}, k) \tag{27}$$

3.1.3.3. Model predictive control algorithm

The objectives of the MPC control algorithm are the following:

- Obtain the desired output load current fixed by the reference.
- Minimize the DC-link capacitor voltage drift.

To deal with these constraints, a cost function is build, whose objective is to minimize the quadratic error, between the reference and the predicted value of the state variable $x[k+1]$, given a switching state S_i. The cost function g_i can be expressed as in Eq. (28):

$$g_i = w_1 \sum_{i=1}^{n} \left(i_s^{*(\alpha\beta)}[k+1] - i_s^{(\alpha\beta)}[k+1] \right)^2 + w_2 \sum_{i=1}^{n} \left(v_{dc(\ell)}^{*}[k+1] - v_{dc(\ell)}[k+1] \right)^2 \tag{28}$$

In Eq. (28), w_1 and w_2 are weighting factors used to give the priority to the control the state variables and must be adjusted for each system in particular. The switching state to be synthesized S_n will result from the optimization of the cast function g_n given as in (29)

$$S_i = min\{g_i\} \tag{29}$$

Using the predictive model for the system state variables given in Eqs. (24) and (26), and the cost function optimization presented in Eqs. (28) and (29), the MPC algorithm can be constructed as the flow diagram presented in **Figures 15** and **16**.

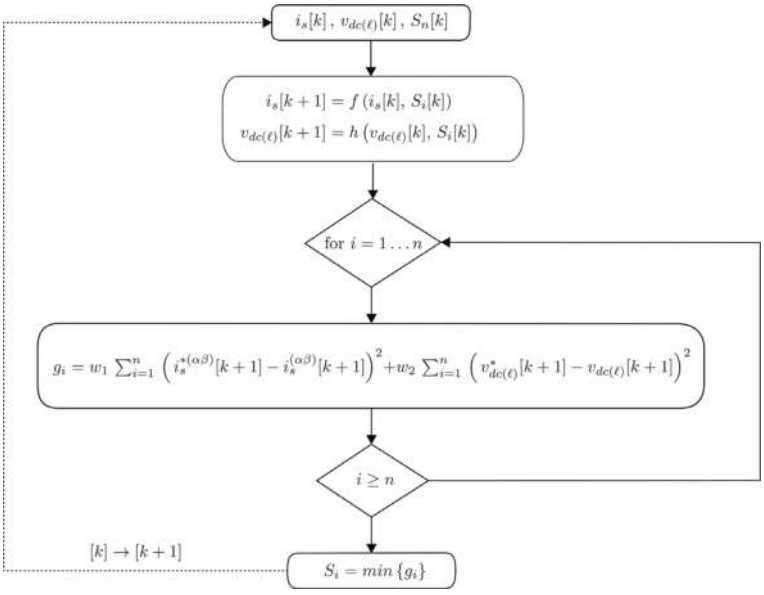

Figure 15. MPC algorithm.

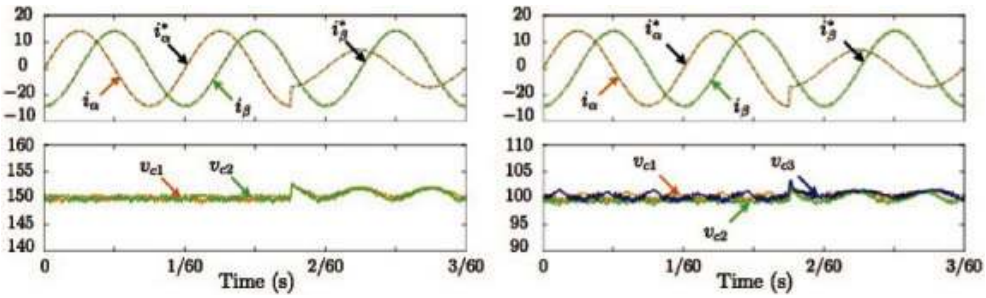

Figure 16. MPC simulation results.

3.1.4. The direct power control approach

Direct power control strategy is based on the power flow balance between the power source, e.g. the wind turbine generator system, and the output power, which is demanded by the grid and the power stored in the DC-link interface. So, the apparent power is known to be as in Eqs. (30) and (31):

$$S = v\,i^{*} \tag{30}$$

$$S = p + jq \tag{31}$$

Active and reactive power components can be written in the $\alpha\beta$ stationary reference frame as in Eq. (32):

$$\begin{cases} P_s = v_s^{\alpha} i_s^{\alpha} + v_s^{\beta} i_s^{\beta} \\ Q_s = v_s^{\alpha} i_s^{\beta} - v_s^{\beta} i_s^{\alpha} \end{cases} \tag{32}$$

Active and reactive power flow is given by the instantaneous variation of active and reactive power as written in Eq. (33):

$$\begin{cases} \dfrac{d}{dt}P_s = v_s^{\alpha}\dfrac{d}{dt}i_s^{\alpha} + i_s^{\alpha}\dfrac{d}{dt}v_s^{\alpha} + v_s^{\beta}\dfrac{d}{dt}i_s^{\beta} + i_s^{\beta}\dfrac{d}{dt}v_s^{\beta} \\ \dfrac{d}{dt}Q_s = v_s^{\alpha}\dfrac{d}{dt}i_s^{\beta} + i_s^{\alpha}\dfrac{d}{dt}v_s^{\beta} - v_s^{\beta}\dfrac{d}{dt}i_s^{\alpha} - -i_s^{\beta}\dfrac{d}{dt}v_s^{\alpha} \end{cases} \tag{33}$$

The power stored in the DC-link capacitor is given Eq. (34):

$$S_{dc} = v_d\, S_k \;\; i_s \tag{34}$$

where S_k stands for the switching state vector of the converter and can be defined as in Eq. (35):

$$S_k = [S_1\; S_2\; S_3]^T \tag{35}$$

In the case of the NPC converter, S_k is represented per phase, so $k \in \{a, b, c\}$.

The DC-link voltage dynamics can be written as in Eq. (36), so

$$C\frac{d}{dt}v_c = S_k i \tag{36}$$

The generator can be considered as a symmetrical three-phase voltage source, so the corresponding voltages in the stationary reference frame $\alpha\beta$ are to be found as Eqs. (37) and (38):

$$v_\alpha = \widehat{V}_s \sin(\omega t) \tag{37}$$

$$v_\beta = -\widehat{V}_s \sin(\omega t) \tag{38}$$

Active and reactive power dynamics can be computed using Eq. (33) and taken the converter-grid model presented in Eq. (15) into consideration, building the following model, based on the power flow:

$$P[k+1] = P[k] + f_{pi}[k]\,T_s \tag{39}$$

$$Q[k+1] = Q[k] + f_{qi}[k]\,T_s \tag{40}$$

4. New converter topologies for WECS

Since most WECS operate in low voltage, they require parallel connection of several converters to be able to handle all the power. An alternative to parallel connection has been adopted by mainstream manufacturers by providing multiple three-phase winding outputs of the generator enabling the connection of back-to-back converters as independent channels to the grid. In this field of application, the dual three-phase generator or multiple three-phase winding generators have become a popular solution.

As presented previously, multichannel configurations are commonly based on 3L-NPC topologies, which introduce DC voltage drift and a linear increasing number of semiconductors and capacitors as function of the number of channels (number of multiple generator windings). These facts introduce the idea of new converter topologies, capable of handling multiple three-phase groups, at the same time, with a single DC-link.

In this line of research, a nine-switch back-to-back topology for wind energy conversion system, as shown in **Figure 17**, is proposed [17–19]. The topology is derived from two three-phase voltage source converters that share a positive and a negative busbar, respectively. Hence three switches are eliminated of the 12 needed for a back-to-back configuration. This comes at expense of some forbidden switching states and limitations in the modulation index of one of the converters, which depends on the difference of the input and output converter frequencies.

4.1. Converter modulation

Unlike the conventional 12-switch back-to-back converter topology, the 9-switch topology introduces some restrictions for the rectifier and inverter modulation. The allowed switching states per leg referred to rectifying stage of the converter **Figure 18** are shown in **Table 4**.

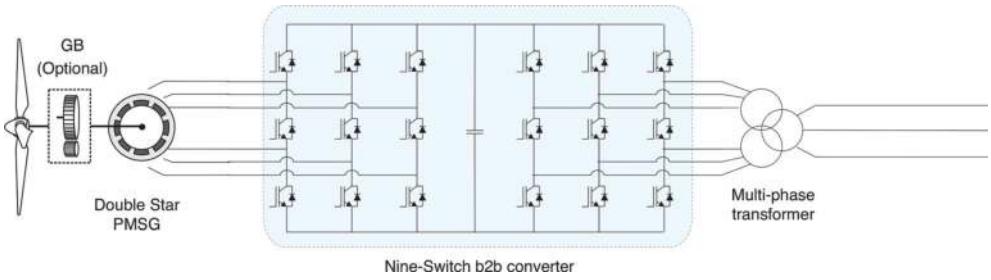

Figure 17. Nine-switch converter back-to-back topology.

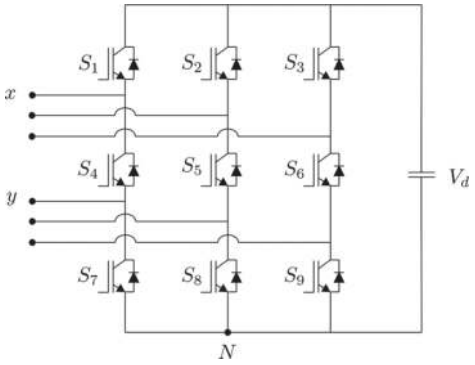

Figure 18. Nine-switch converter topology, rectifying stage.

S_1	S_4	S_7	v_{xN}	v_{yN}
	1	0	V_d	V_d
	0	0	0	0
	0	1	V_d	0

Table 4. Allowed switching states (one leg shown).

The modulation strategy proposed is a classical 12-switch back-to-back converter PWM modulation, where the restrictions for the middle switches are obtained from **Figure 19** and implemented as follows:

$$S_j = \overline{S}_{j-3} \oplus S_{j+3} \quad \forall j \in [4,5,6] \tag{41}$$

Thus, the DC-link enables the decoupling of the generator and grid side, then constant frequency mode modulation scheme can be implemented; thus, both voltage reference space vectors having a constant phase shifting angle δ will always to be found at least in contiguous sectors; then in this case, the maximum modulation index is given by Eq. (42):

$$m = \frac{1}{\sqrt{3}} \tag{42}$$

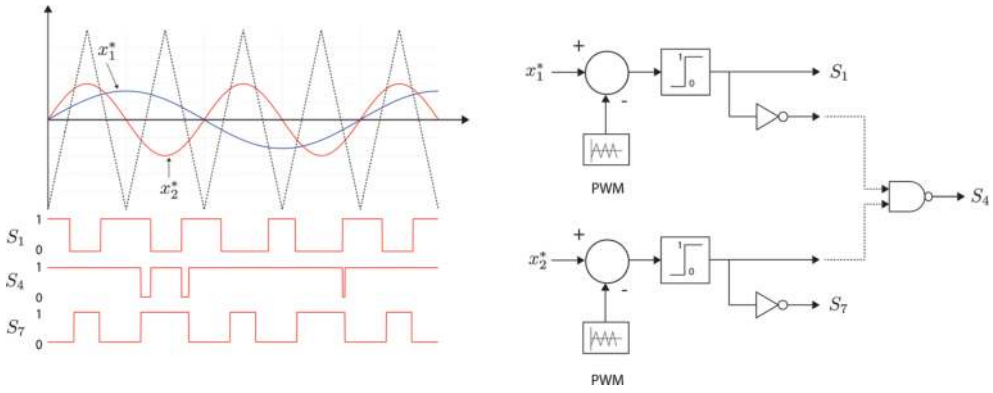

Figure 19. Nine-switch converter modulation strategy implementation.

4.2. DC-link voltage control

DC-link voltage control is achieved using a modified structure of the active and reactive control scheme presented in Eqs. (2)–(3) in Section 2.2 of this chapter.

A virtual flux-oriented control (VFOC) strategy with active and reactive control is implemented for each inverter output. The active power delivered by the inverter is used to control the DC-link capacitor voltage, while the reactive power is set on each three-phase output group to obtain unity power factor operation, just as a common back-to-back VSC. The control implementation for one channel is shown in **Figure 20**.

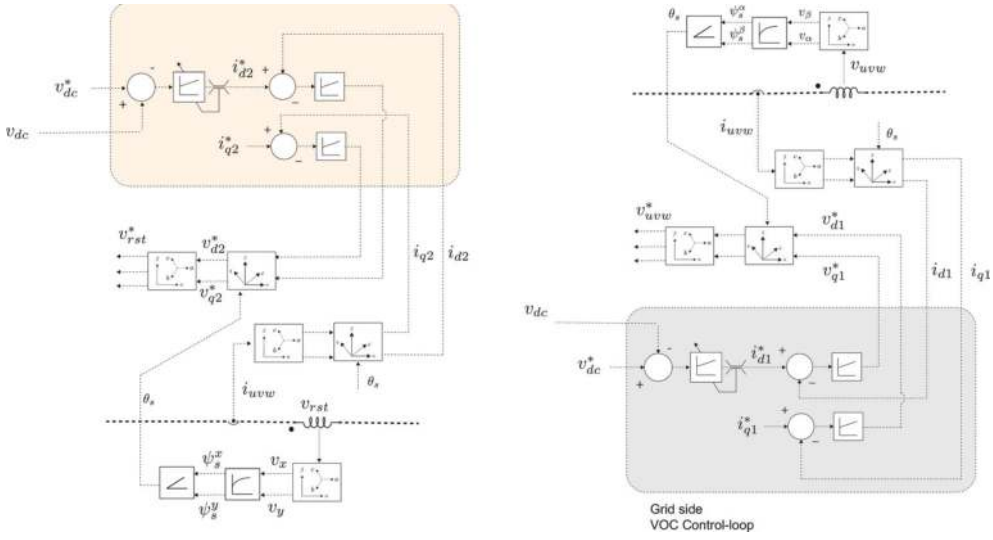

Figure 20. Nine-switch converter grid side control scheme.

Results for the generator side performance are shown in **Figure 21**. In **Figure 21(a)** and **(b)**, during the speed step-up, no electrical torque is produced, thus allowing the mechanical torque to speed up the generator as shown in **Figure 21(a)**. Once the wind turbine reaches the speed reference ω_r^* provided by the MPPT controller, the electrical torque starts to build up, until it reaches the desired setting point, converging to its steady state; the FOC outer loop PI controller ensures zero steady-state speed error, while the inner control loop ensures i_q current, hence mechanical torque tracking.

In **Figure 22**, a derivation of the previously topology is presented, but in a multiphase, multichannel configuration, so each nine-switch converter is providing dual power flow. This fact forces the converter to operate in VFM modulation mode, thus reducing the DC-link modulation index.

4.3. Future work

The nine-switch converter topology has proven to have many advantages to deal with multiphase, multichannel WECS configurations, by having the ability to manage simultaneously different voltage space vector references in a single DC-link capacitor. This feature ensures a simple control scheme, based in active and reactive power control.

Future work on this converter topology includes the research on MBPC and sliding mode control of the nine-switch converter in back-to-back and bidirectional configurations.

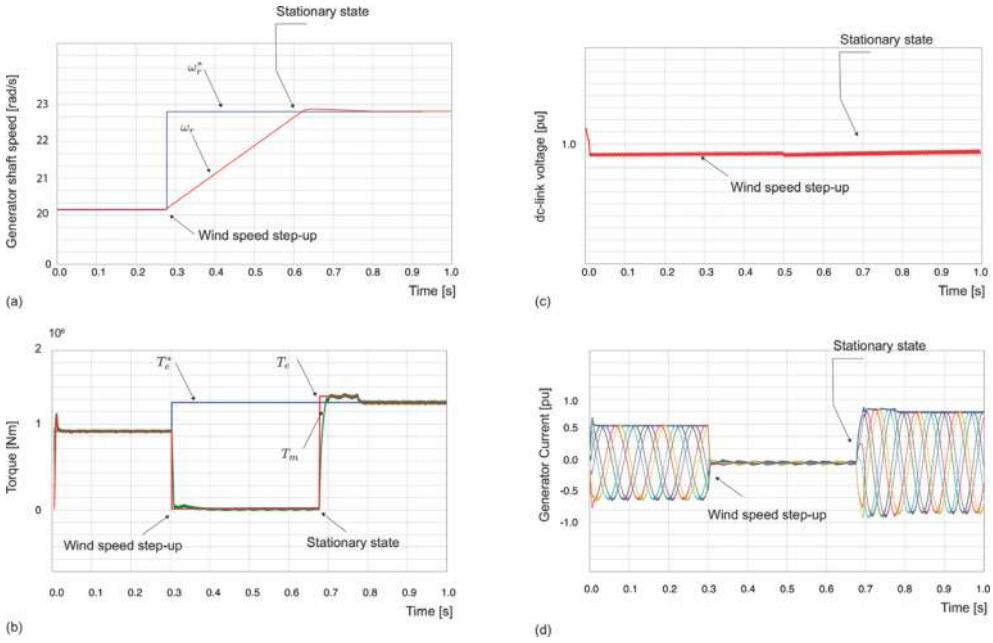

Figure 21. Generator side simulation results: (a) rotor speed, (b) torque, (c) DC-link voltage and (d) generator side currents.

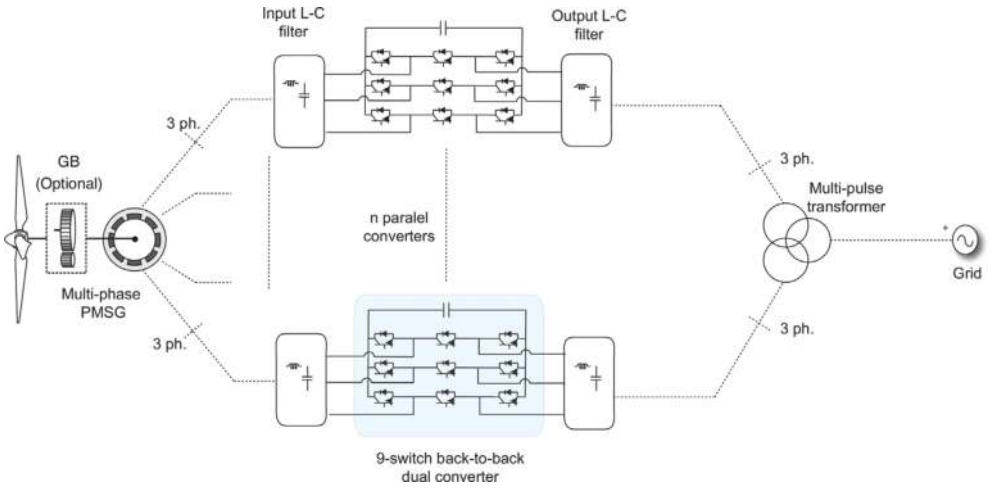

Figure 22. Multichannel nine-switch converter topology.

5. Conclusions

In this chapter, an overview on WECS is presented with the main focus on full-scale power converters employed with a squirrel cage, permanent magnet and wound rotor synchronous generators. With the combination of different types of generators and power converters, a variety of WECS configurations have been investigated. Various technical issues related to CHB and NPC multilevel converter configurations were discussed referred to their DC-link voltage stability as function of its modulation scheme.

The operating principle of the FCS-MPC strategy is presented for ideal and implementation cases. The cost function flexibility and potentiality in achieving different control and technical requirements are discussed. The generalized approach based on FS-MPC strategy has been presented for multilevel NPC converters. The dynamics of the load/grid currents and DC-link capacitor voltages are formulated as a function of switching states and the mathematical prediction model of the converter. The proper selection of the switching states leads to the minimization of the cost function. It has to be noted that the weighting factors assigned to each term on the cost function are dependent on the operational requirements and the stability of the mathematical model. The proposed method shows an intuitive and promising approach to balance the DC-link capacitor voltages, even with the perturbations in the system model.

The main drawback of NPC converter topologies is the requirement of neutral point current compensation, due to the natural path established in some switching states. On the other hand, for CHB converter topologies, no neutral point current is allowed to flow, due to its floating neutral condition, leading to DC-link voltage stability.

DC-link voltage stability is hardly related not only to the grid side active and reactive power demands and voltage symmetry but also to the power converter topology and modulation

strategy. As presented, neutral point clamped topologies are more attractive from the point of view of the multilevel voltage output wave form, which has better performance in terms of THD and grid code compatibility. On the other side, H-Bridge-based topologies present a better DC-voltage stability and simpler control schemes. In these fields, the nine-switch converter appears as suitable alternative. An extensive study with the implementation of MPC and sliding mode control for the nine-switch topology has to be undertaken, to evaluate its performance under grid fault operation and to evaluate restricted switching states and voltage stability.

Author details

Carlos A. Reusser

Address all correspondence to: carlos.reusser@usm.cl

Department of Electronics, Universidad Tecnica Federico Santa Maria, Valparaiso, Chile

References

[1] W. E. Council. World Energy Resources 2013 Survey. World Energy Council. 2013; pp. 1-468

[2] REN21. Renewable Energy Policy Networks for the 21st Century. Renewables 2014 Global Status Report. 2015. www.ren21.net

[3] Wu B, Lang Y, Zagari N, Kouro S. Power Conversion and Control of Wind Energy Systems. Vol. 24. Wiley-IEEE Press; Aug 6, 2011. ISBN-10: 0470593652; ISBN-13: 978-0470593653

[4] Blaabjerg F, Liserre M, Ma K. Power electronics converters for wind turbine systems. IEEE Transactions on Industry Applications. March-April 2012;**48**(2):281-290

[5] Lubosny Z. Wind Turbine Operation in Electric Power Systems: Advanced Modeling, Vol. 1. Springer; December 2010

[6] Teodorescu R, Liserre M, Rodriguez P. Grid Converter Structures for Wind Turbine Systems. Wiley-IEEE Press; 2011. pp. 123-143

[7] Kouro S, Malinowski M, Gopakumar K, Pou J, Franquelo LG, Wu B, Rodriguez J, Perez MA, Leon JI. Recent advances and industrial applications of multilevel converters. IEEE Transactions on Industrial Electronics. Aug 2010;**57**(8):2553-2580

[8] Rodriguez J, Rivera M, Kolar J, Wheeler P. A review of control and modulation methods for matrix converters. IEEE Transactions on Industrial Electronics. Jan 2012;**59**(1):58-70

[9] Thongam JS, Bouchard P, Ezzaidi H, Ouhrouche M. Wind speed sensorless maximum power point tracking control of variable speed wind energy conversion systems. In: 2009

IEEE International Electric Machines and Drives Conference. Miami, FL; 2009. pp. 1832-1837. DOI: 10.1109/IEMDC.2009.5075452

[10] Srighakollapu N, Sensarma P. Sensorless maximum power point tracking control in wind energy generation using permanent magnet synchronous generator, 2008 34th Annual Conference of IEEE Industrial Electronics. Orlando, FL; 2008. pp. 2225-2230

[11] Malinowski M, Kazmierkowski M, Trzynadlowski A. A comparative study of control techniques for pwm rectifiers in ac adjustable speed drives. IEEE Transactions on Power Electronics. Nov 2003;**18**(6):1390-1396

[12] Busca C, Stan A-I, Stanciu T, Stroe D. Control of permanent magnet synchronous generator for large wind turbines. In: 2010 IEEE International Symposium on Industrial Electronics (ISIE); July 2010. pp. 3871-3876

[13] Tolbert LM, Peng FZ, Habetler TG. Multilevel pwm methods at low modulation indices. IEEE Transactions on Power Electronics. Jul 2000;**15**(4):719-725

[14] Bin W. High-Power Converters and AC Drives. 1st ed. Wiley-IEEE Press; 2006. pp. 1-468

[15] Shu Z, He X, Wang Z, Qiu D, Jing Y. Voltage balancing approaches for diode-clamped multilevel converters using auxiliary capacitor-based circuits. IEEE Transactions on Power Electronics. May 2013;**28**(5):2111-2124

[16] Busquets-Monge S, Bordonau J, Rocabert J. A virtual-vector pulsewidth modulation for the four-level diode-clamped dc–ac converter. IEEE Transactions on Power Electronics. July 2008;**23**(4):1964-1972

[17] Reusser CA, Kouro S. Nine switch multi-channel dual converter for WECS. In: 41st Annual Conference of the IEEE Industrial Electronics Society, IECON 2015; Nov 2015. pp. 005363-005368

[18] Reusser CA, Kouro S. Back-to-back wind energy conversion system configuration based on 9-switch dual converter and open-end-winding PMSG. In: 2015 IEEE 13th Brazilian Power Electronics Conference and 1st Southern Power Electronics Conference (COBEP/SPEC); Nov 2015. pp. 1-6

[19] Reusser CA, Kouro S, Cardenas R. Dual three-phase pmsg based wind energy conversion system using 9-switch dual converter. In: 2015 IEEE Energy Conversion Congress and Exposition (ECCE); Sept 2015. pp. 1021-1022